Paleomagnetic study of impactites from the Karla impact structure suggests protracted postimpact hydrothermalism

Dilyara Kuzina, Jérôme Gattacceca, Natalia Bezaeva, Dmitry Badyukov, Pierre Rochette, Yoann Quesnel, François Demory, Daniel Borschneck

The Meteoritical Society

Meteoritics & Planetary Science 1–15 (2022)
doi: 10.1111/maps.13906

Paleomagnetic study of impactites from the Karla impact structure suggests protracted postimpact hydrothermalism

Dilyara M. KUZINA[1], Jérôme GATTACCECA[2]*, Natalia S. BEZAEVA[3], Dmitry D. BADYUKOV[3], Pierre ROCHETTE[2], Yoann QUESNEL[2], François DEMORY[2], and Daniel BORSCHNECK[2]

[1]Institute of Geology and Petroleum Technologies, Kazan Federal University, 4/5 Kremlyovskaya Str, 420008 Kazan, Russia
[2]CNRS, Aix Marseille Univ, IRD, INRAE, Aix-en-Provence, France
[3]Vernadsky Institute of Geochemistry and Analytical Chemistry, Russian Academy of Sciences, 19 Kosygin Str, 119991 Moscow, Russia
*Corresponding author. E-mail: gattacceca@cerege.fr

(Received 16 June 2021)

Abstract–We present a paleomagnetic study of the ~10 km diameter Karla impact structure in Russia. We sampled the target carbonate rocks, and a yet undocumented fragmental melt-bearing lithic breccia layer. This impact breccia, which contains carbonate melt, is enriched in stoichiometric magnetite by a factor of ~15 compared to the target lithologies, and carries a stable natural remanent magnetization. The weak remanent magnetization and the presence of both normal and reverse polarities down to the centimeter scale indicate that the breccia does not carry a thermoremanent magnetization (TRM), but rather a chemical remanent magnetization (CRM). The presence of stoichiometric magnetite and the absence of TRM suggest that the magnetite was formed during relatively low-temperature postimpact hydrothermalism that affected the porous impact breccia layer. During this process, the breccia acquired a CRM. The paleomagnetic direction is compatible with a Cenozoic age for the impact event, but cannot bring more precise constraint on the age because of the stable position of the Eurasian plate over the last 60 Myr. However, the presence of both polarities indicates that mild hydrothermalism took place over a period of time long enough to span at least one reversal of the geomagnetic field, that is, over a time scale of the order of 100 kyr. This confirms that protracted hydrothermal systems associated with impact craters are long lived, even in relatively small craters such as Karla, and are key features of the geologic and environmental effects of impacts on Earth.

INTRODUCTION

Hypervelocity impacts are a major evolution process of solar system solid bodies (Melosh, 2002; Osinski & Pierazzo, 2012). Planets, satellites, asteroids, and comets all display impact craters that are the memory of their collisional history. On Earth, this memory is mostly erased by geological activity, but over 200 impact craters (also called impact structure when the crater is eroded or buried) have been identified so far (Schmieder & Kring, 2020). The geology of impact craters is not limited to their formation and their erosion. Impact craters have been shown to host hydrothermal systems that could have provided hospitable environments for the appearance of life, or at least its recovery following the devastating effects of the impact itself on the biosphere (e.g., Osinski et al., 2012).

Such hydrothermal systems have been evidenced by petrography (e.g., Kring et al., 2020; Simpson et al., 2020) and geophysics (e.g., Escobar-Sanchez & Urrutia-Fucugauchi, 2010; Pilkington & Hildebrand, 2000; Quesnel et al., 2013; Zylberman et al., 2017). They are favored by the residual heat from the impact event, with the presence of a layer of molten rock in the largest

craters (e.g., Dressler & Reimold, 2001), the presence of water (either seawater for submarine impacts or formation of a lake filling the crater in continental settings), and the increased porosity of some impact-processed rocks (fractured target rocks and impact generated breccia). Modeling suggests that these hydrothermal systems can be long-lived, with activity over the Myr time scale for large craters such as the 150 km diameter Chicxulub crater (e.g., Abramov & Kring, 2007), which is a key aspect of their capacity to host life. However, observational evidence for the occurrence of protracted hydrothermal activity is scarce.

Hydrothermal activity lasting for about 250 kyr has been evidenced for the 24 km diameter Ries crater based on the study of a travertine mound formed following the impact (Arp et al., 2013). Paleomagnetic study of impact breccia has been used recently to evidence the long duration of the hydrothermal system associated with the 150 km diameter Chicxulub impact crater (Kring et al., 2020). By revealing that the breccia was remagnetized by hydrothermalism over at least one reversal of the geomagnetic field, this study allowed setting a minimum duration of 150 kyr, in agreement with thermal modeling. In this work, we present the results of a paleomagnetic study of the impact breccia and the target rocks from the smaller, ~10 km diameter, Karla impact structure in Russia, and discuss their implication for the postimpact processes that have affected this crater.

GEOLOGICAL SETTING

The Karla impact structure spans across the border of Tatarstan and Chouvash Republics (Federation of Russia) and is centered at 54°56.9′N 47°56.5′E, about 120 km SSW of the city of Kazan. This structure was first described as an impact structure in the 1970s (Masaitis et al., 1976, 1980) and recently revisited with a focus on geophysics (Quesnel et al., 2022). Although the regional geological map still favors a tectonic origin for the structure (Semakin et al., 1999), the occurrence of well-developed shatter cones leaves no doubt about the impact origin of the structure (Masaitis et al., 1976; Quesnel et al., 2022).

The Karla impact structure has a poorly constrained diameter of about 10 km according to Masaitis (1999), within a 6–12 km range according to Quesnel et al. (2022). The target rocks are Devonian to Cretaceous carbonate rocks with a total thickness of 1.7 km and a subhorizontal bedding, overlying the Archean gneissic basement (Semakin et al., 1999). Surface formations surrounding the crater are Cretaceous and Jurassic. The impact structure has a central uplift made of brecciated Permian and upper Carboniferous limestones. The existence of a central uplift was first evidenced by drilling (Semakin et al., 1999) and confirmed by geophysics (Quesnel et al., 2022). This uplift is surrounded by crater fill deposits ("allogenic breccia" of Masaitis, 1999; Masaitis et al., 1980) consisting of mega-blocks (up to 1 km) of middle Carboniferous to upper Cretaceous carbonate rocks set in a clastic matrix of the same lithologies, with a maximum thickness of 500 m. It is overlain by a thin distinct layer of fine-grained porous impact breccia containing centimetric mostly carbonate clasts that was not described in the geological map (Semakin et al., 1999) or in the general description of the crater (Masaitis, 1999; Masaitis et al., 1976, 1980). This breccia is locally injected as dikes into the central uplift rocks. We describe this impact breccia in more detail in the Geology and Petrography section. These formations are covered by Pliocene lacustrine deposits with maximum thickness 100 m that sedimented in the lake that filled the crater, and ultimately by Quaternary deposits.

An age of 5 ± 1 Ma was proposed for the crater, based on biostratigraphic data (Masaitis et al., 1980). However, as discussed in more detail in Quesnel et al. (2022), although the Pliocene age of the lacustrine sediments filling the crater sets a younger limit of about 4 Ma for the age of the impact, the older limit is based only on the brief mention of the presence in the allogenic breccia formation of opoka clasts of Syzranian age (Masaitis et al., 1980), later described as "opoka fragments of Miocene age" in Masaitis (1999), whereas the Syzranian stage is in the Paleocene (Gradstein et al., 2020). The age of the structure is therefore only poorly constrained by the stratigraphy, as it could be as old as Paleocene.

SAMPLES AND METHODS

Sampling

The overall flat morphology makes outcrops scarce within the Karla impact structure. Only eight sites were sampled for paleomagnetism, mostly in quarries near the Karla river (Fig. 1). We collected an average of nine oriented cores per site. Four sites were sampled in the impact breccia (KAR01, 04, 05, 08). Four sites were sampled in the brecciated target carbonate rocks: two in the central uplift (KAR02, 03) and two in the allogenic breccia deposits (KAR06, 07). Sampling for paleomagnetism was performed by drilling 2.5 cm diameter cores with a gas-powered drill. The cores were oriented using a magnetic compass. They were cut into 2.2 cm high cylinders for the paleomagnetic analyses. At a few sites where the impact breccia was present only as loose unoriented blocks, unoriented hand samples were also collected for the study of intrinsic magnetic properties and petrography (KAR15, 16, 18, 19).

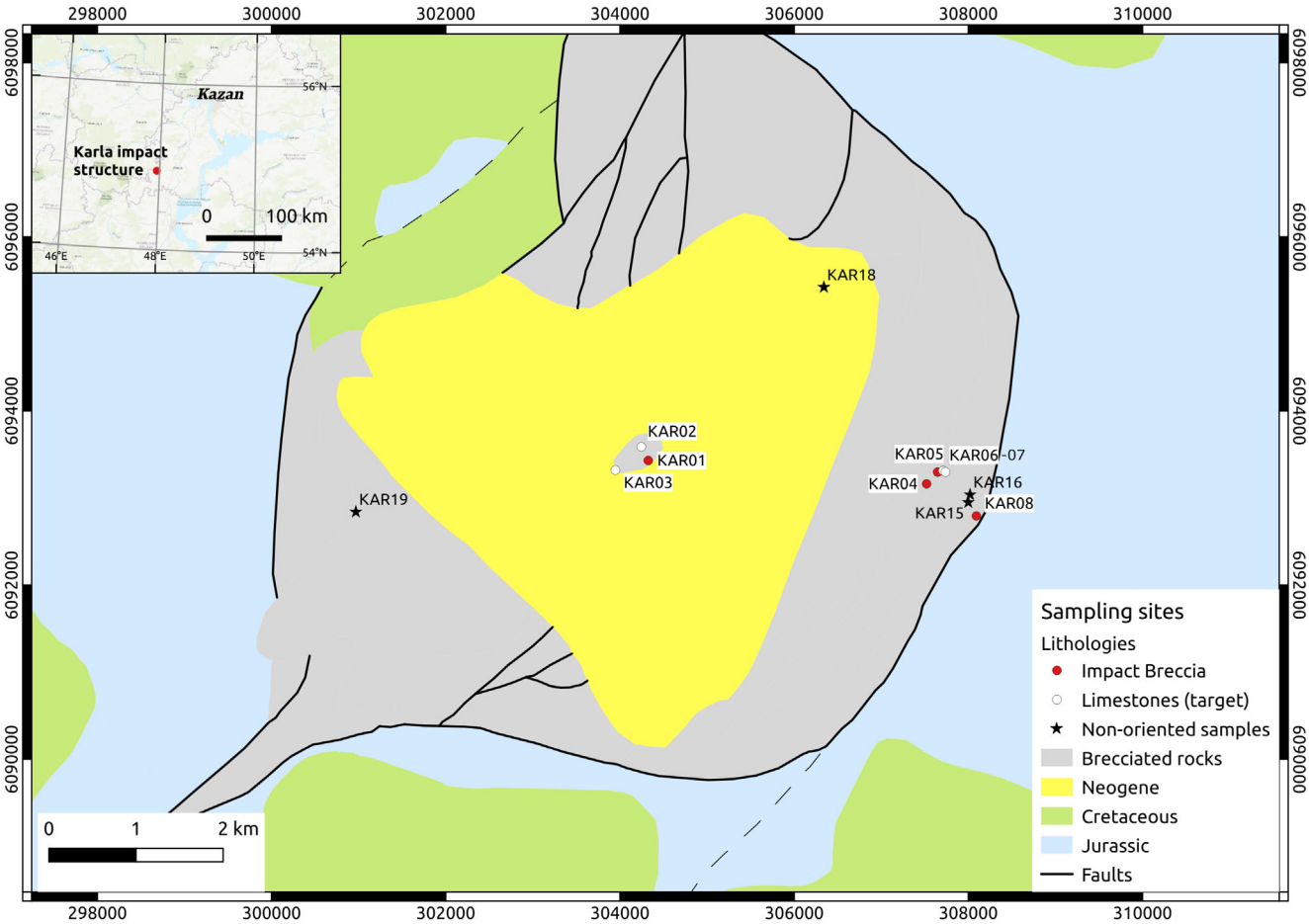

Fig. 1. Maps of sampled localities. The simplified geological map is from Masaitis (1999).

Petrography

Petrographic observations were conducted using a Leica DM2500P petrographic microscope at CEREGE, and a field emission gun scanning electron microscope (SEM) Tescan Mira3 operated at 20 kV and equipped with energy-dispersive spectrometry (EDS) at the Vernadsky Institute. X-ray diffraction analyses were performed at CEREGE using a Panalytical X'Pert PRO X-ray diffractometer equipped with a Cobalt source (λ = 1.79 Å) running at 40 kV and 40 mA. Each sample was scanned from 5° to 75° (2θ) with a step size of 0.033° at a total counting time of 2 h. Samples were ground in an agate mortar, deposited on low background silicon plates with a drop of ethanol to make a thin and homogeneous layer of powder. Samples were also spun at 15 rpm during measurement to bring more crystallographic planes into diffraction condition, thus improving the diffraction pattern statistics. The identification of the minerals was performed using the ICDD PDF-2 database. All raw diffraction data as well as diffraction patterns with mineral peaks identification are provided in the supporting information (Data S1).

The bulk porosity was determined at CEREGE by measuring the grain density and the bulk density. Grain density was measured with a Quantachrome Helium stereopycnometer. Bulk density was determined by measuring the volume (with a caliper) and the mass of cylindrical samples.

Rock Magnetism and Paleomagnetism

All magnetic measurements were performed at CEREGE. Low-field magnetic susceptibility was measured using an MFK1 Kappabridge instrument (operating at 200 A m^{-1} peak field and 976 Hz frequency, with sensitivity of 5 × 10^{-13} m^3). Thermal demagnetizations of natural remanent magnetization (NRM), isothermal remanent magnetization (IRM), and anhysteretic remanent magnetization (ARM) were conducted using an MMTD furnace. For the thermal demagnetization of IRM, samples were given a 3 T IRM along one axis and then a 0.1 T

IRM along an orthogonal axis, using a MMPM9 pulse magnetizer from Magnetic Measurements. This procedure enables monitoring separately the thermal demagnetization of the high- and low-coercivity grains. ARM was imparted using an alternating field (AF) field of 200 mT and a bias field of 100 μT with an LDA5 instrument from Agico. Hysteresis properties (saturation remanence M_{RS}, saturation magnetization M_S, coercivity B_C, coercivity of remanence B_{CR}) were measured with two vibrating sample magnetometers: a Princeton MicroMag 3900 model and a Lakeshore 8604 model. Both instruments have a sensitivity of ~10^{-8} Am^2. The saturation magnetization was estimated from the hysteresis loops after correction for the high-field susceptibility computed for fields higher than 0.5 T.

All remanence measurements were performed with a SQUID magnetometer (2G Enterprises, model 760R, with noise level of 10^{-11} Am^2) in a magnetically shielded room, with an attached automated three-axis AF degausser system. For each site, pilot samples were studied using thermal and AF demagnetization in order to select the best demagnetization protocol for the remaining samples.

Demagnetization data were analyzed through principal component analysis (Kirschvink, 1980) using PaleoMac software (Cogné, 2003). To compute average directions, we use the statistical approach of Fisher (1953) with parameters k (precision parameter) and α_{95} (semiaperture of the 95% confidence cone around the average direction).

RESULTS

Geology and Petrography

The rocks sampled in the target carbonate rocks (sites KAR02, 03, 06, 07) consist of fine-grained limestones of varied age (Carboniferous to Permian). The four other sites that were studied for paleomagnetism consist of impact breccia. This breccia has a subhorizontal bedding and was observed up to 4 km from the center of the impact structure (site KAR08 in Fig. 1). Its maximum observed thickness is 15 m at site KAR08. The breccia consists of a fine-grained groundmass with about 10 vol% of clasts (Fig. 2). Its groundmass is porous, homogeneous, and has a white color in hand specimens. The clasts are mostly heterometric, angular to subangular, lithic clasts of limestone, more rarely dolomite. Rounded clasts made of clayish material are locally present, especially in the eastern part of the structure, around site KAR08. The clast size is up to 2 cm. Angular mineral clasts in the matrix are represented mainly by calcite and quartz, with lesser amounts of feldspar (albite and K-feldspar). The boundaries between the clasts and matrix are sharp, with no apparent traces of recrystallization or alteration present at the clast rims (Fig. 3a). The breccia matrix is fine-grained, has equigranular texture, and consists entirely of euhedral crystals of calcite ranging in size from 1 to 5 μm (Fig. 3b).

X-ray diffraction analyses of a bulk breccia sample from site KAR08 reveal the presence of mostly calcite, dolomite, and quartz. Albite is possibly present, but only the main peak at 3.19 Å (32.53° 2θ) was detected. Traces of clays are detected with a peak around 15 Å (6–7° 2θ) corresponding to the basal diffraction peak of smectite, and a peak around 4.4 Å (23° 2θ) that is a (hk0) peak of smectite. This latter peak could correspond to other clays (chlorite, kaolinite, illite), but their basal peak was not detected, so we favor the smectite interpretation.

Three bulk breccia samples of about 300 g, from sites KAR01, KAR08, and from a loose breccia boulder collected about 1 km north of site KAR 01, were dissolved in HCl to better constrain the mineralogy of the noncarbonated fraction. X-ray diffraction analyses of the residues evidenced quartz, feldspar (orthose and albite). A broad peak between 6° and 7° (2θ), like in the bulk breccia but with a higher intensity, can be attributed to a smectitic clay even if the exact type of the clay cannot be identified. The main peak of micas is detected at 9.98 Å (10° 2θ), and attributed to muscovite because most of the other diffraction peaks of muscovite are also detected. However, the peaks are of low intensities, and minerals belonging to the mica family are numerous and have relatively close diffraction peaks. Therefore, the identification remains hypothetical. The main peak of kaolinite is detected at 7.17 Å (14.3° 2θ). It is a very low-intensity peak, so the identification is hypothetical as well. The main diffraction peaks of gypsum and bassanite are identified at 13.5 Å (7.6° 2θ) and 3.0 Å (34.6° 2θ), respectively. Their intensities are low, but other peaks from these two minerals are also detected.

We measured a bulk porosity of 31 ± 3% on five impact breccia samples of masses about 20 g (detailed data are provided in Table S1 in supporting information). From the secondary electron images of polished samples, the porosity of the matrix is estimated to be 10–15%, with pore size from a few millimeters down to less than 1 μm, and pore shapes from elongated to spherical. This porosity estimate is significantly lower than the 31% porosity measured using helium pycnometry. This discrepancy is due to the fact that pores smaller than about 1 μm were not resolved in the SEM images.

Rock Magnetism

The magnetic properties of the studied rocks are listed in Table 1. In addition to the properties measured

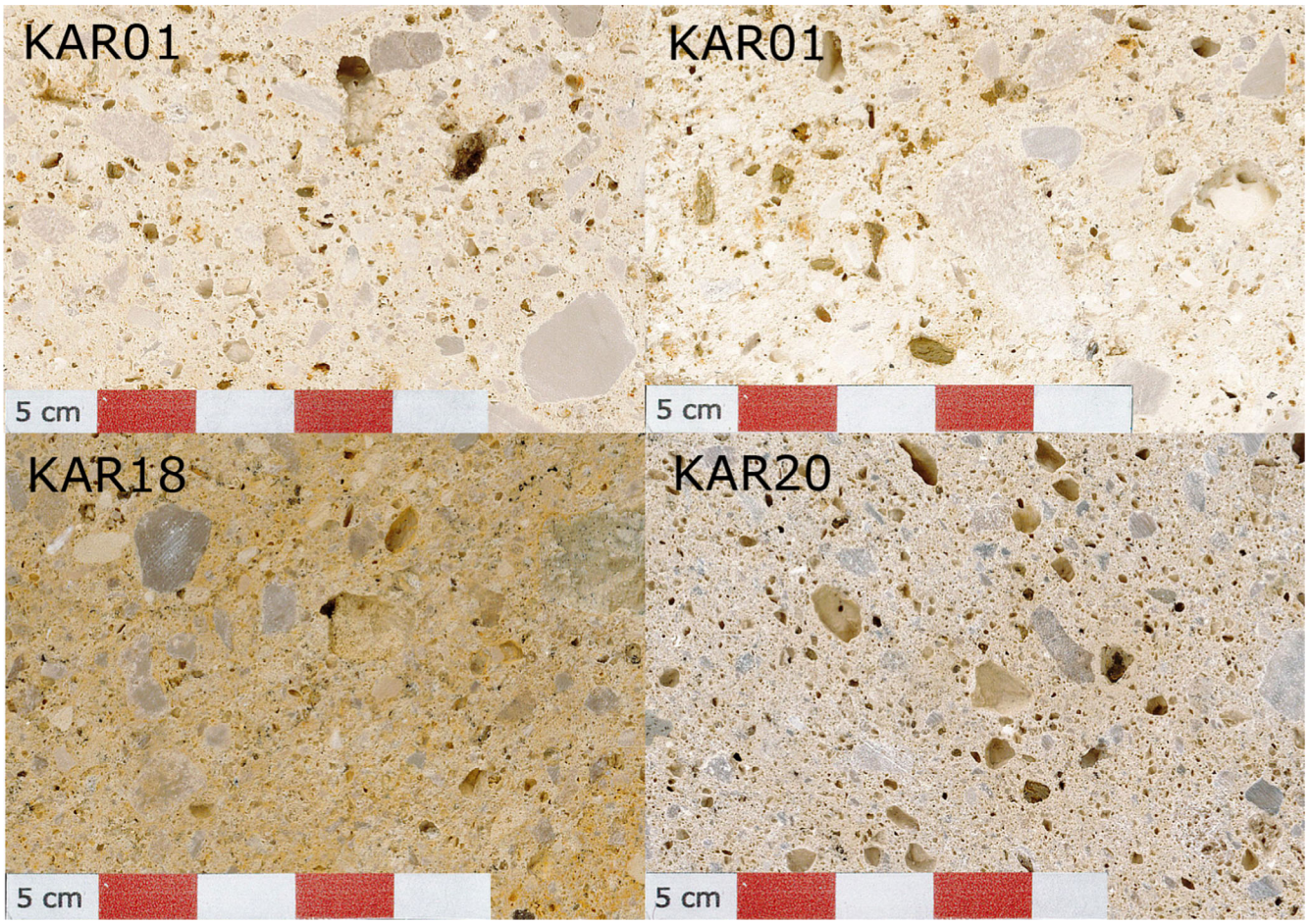

Fig. 2. Macroscopic photographs of the impact melt breccia.

on the drill cores obtained for the paleomagnetic study, a number of additional bulk hand samples were studied. All rocks from Karla structure have a low content of ferromagnetic minerals, as indicated by their near zero to negative magnetic susceptibility. ARM and saturation IRM (sIRM, acquired in a field of 3 T) were measurable in all samples. There is a clear dichotomy between the magnetic properties of limestones and of impact breccia. ARM is 10 times higher, and sIRM is 14 times higher in impact breccia than in limestones. The most magnetic limestone sample is still less magnetic than the least magnetic impact breccia sample.

Thermal demagnetization of IRM and ARM is shown in Fig. 4. The thermal demagnetization of IRM shows a complete demagnetization at 580 °C, typical of stoichiometric magnetite. In two of three samples (kar0810a impact breccia and kar0701b limestone), a faint kink is visible around 325 °C possibly evidencing a small amount of pyrrhotite. Thermal demagnetization of the ARM of impact breccia shows a sharp decrease starting from 480 °C, and complete demagnetization by 580 °C.

AF demagnetization of IRM and ARM is shown in Fig. 5. Less than 10% of the magnetization is left after AF demagnetization at 100 mT. Median destructive field for ARM and IRM in the impact breccia are 36 ± 6 mT and 29 ± 2 mT, respectively. S_{-300} values range from 0.90 in limestones to 0.97 in the impact breccia.

The most magnetic impact breccia is from the easternmost outcrops, around the paleomagnetic site KAR08. We were not able to measure hysteresis properties of bulk breccia or limestone samples because of their low content in ferromagnetic minerals. However, we were able to measure the hysteresis properties of the residues of the dissolution with HCl of a bulk breccia sample from site KAR08 (Fig. 6). Multiple samples for a total mass of 2.46 g of material were measured. The average hysteresis parameters (mass weighed for M_S and M_{RS}) are $M_S = 3.67 \times 10^{-4}$ Am^2 kg^{-1}, $M_{RS} = 7.56 \times 10^{-5}$ Am^2 kg^{-1}, $B_C = 12.6$ mT, $B_{CR} = 38.5$ mT.

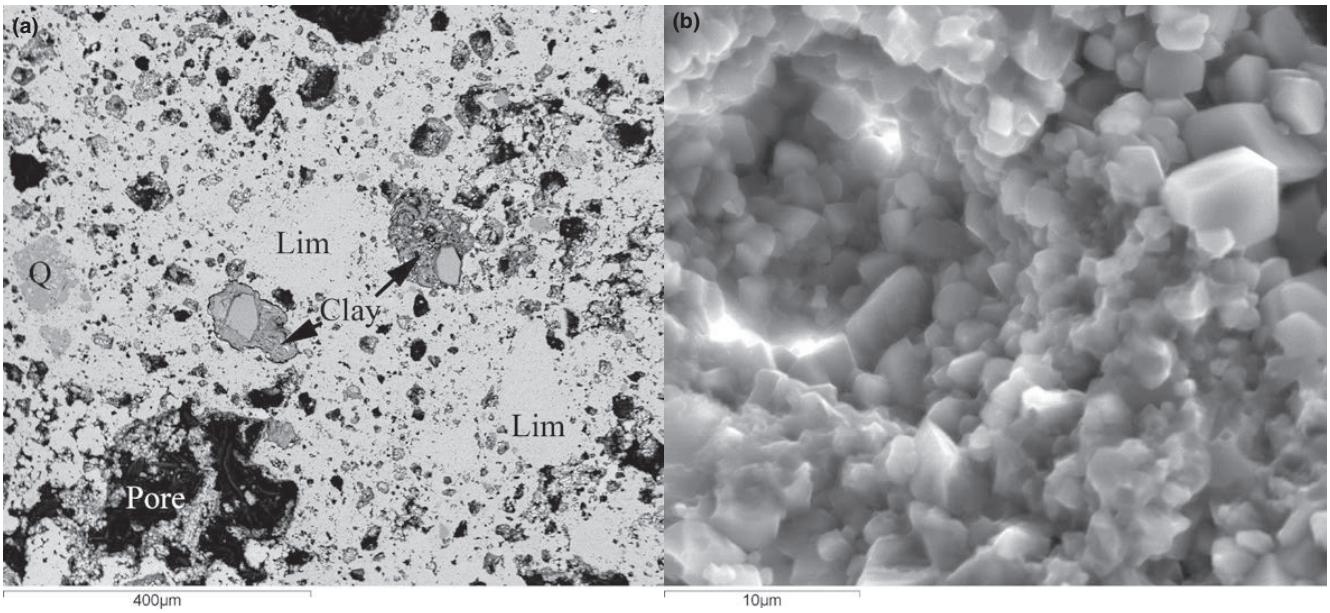

Fig. 3. Petrography of impact melt breccia. a) Backscattered electron image of a polished section. The fine-grained calcite matrix (light gray) with numerous pores (black) includes clasts of limestone (Lim), clay and thermally altered clay inclusions (Clay) with detrital quartz grains (gray), and mineral and lithic clasts (Q). b) Secondary electron image of the matrix of a split surface. The matrix is composed of euhedral calcite crystals and has high porosity.

Table 1. Magnetic properties of rocks from the Karla impact structure.

Rock type	Site	NRM (10^{-8} Am^2 kg^{-1})	n	χ (10^{-9} m^3 kg^{-1})	Mass measured (g)	ARM (10^{-7} Am^2 kg^{-1})	n	sIRM (10^{-6} Am^2 kg^{-1})	n
Impact breccia	KAR01	0.355	10	−2.18	200	1.34	1	1.59	1
Impact breccia	KAR04	1.14	26	−0.199	520	7.69	6	6.27	5
Impact breccia	KAR05	1.10	9	0.815	180	3.19	2	3.59	2
Impact breccia	KAR08	2.70	15	3.60	300	5.94	8	16.6	8
Impact breccia	KAR15*	2.70	1	2.80	102			5.63	1
Impact breccia	KAR16*	1.87	1	−0.238	164			5.66	1
Impact breccia	KAR18*	1.68	4	0.392	49.6			3.20	2
Impact breccia	KAR19*	4.14	2	−2.52	5.8	6.15	2	1.54	2
	Average	1.96	8	0.309	1521	4.86	17	5.51	22
Limestone	KAR02	0.121	5	−3.89	100	0.174	1	0.283	1
Limestone	KAR03	0.430	5	−4.45	100	0.123	1	0.213	1
Limestone	KAR06	0.364	9	1.63	180	1.15	1	1.16	1
Limestone	KAR07	0.473	8	−3.09	160	0.944	1	1.08	2
	Average	0.347	4	−2.45	540	0.598	4	0.685	5

n is the number of measured paleomagnetic specimens (one specimen is about 20 g). Average values are computed at site level with n being the number of sites. For magnetic susceptibility, the measured mass is given instead of the number of specimens or sites. ARM was acquired in a 100 μT bias field and a 120 mT alternating field.
*Sites with no oriented samples.

Paleomagnetism

With an average moment and intensity of $9.1 \pm 6.4 \times 10^{-11}$ Am^2 and $3.63 \pm 2.61 \times 10^{-9}$ Am^2 kg^{-1} ($n = 27$), the NRM of all studied limestone specimens was too weak to allow paleomagnetic study. The NRM of impact breccia specimens is significantly higher, with average moment and intensity of $2.38 \pm 2.41 \times 10^{-10}$ Am^2 and $1.39 \pm 1.36 \times 10^{-8}$ Am^2 kg^{-1} ($n = 60$). However, with a median moment of 1.20×10^{-10} Am^2, most impact breccia samples were still too weakly magnetized to provide relevant paleomagnetic information.

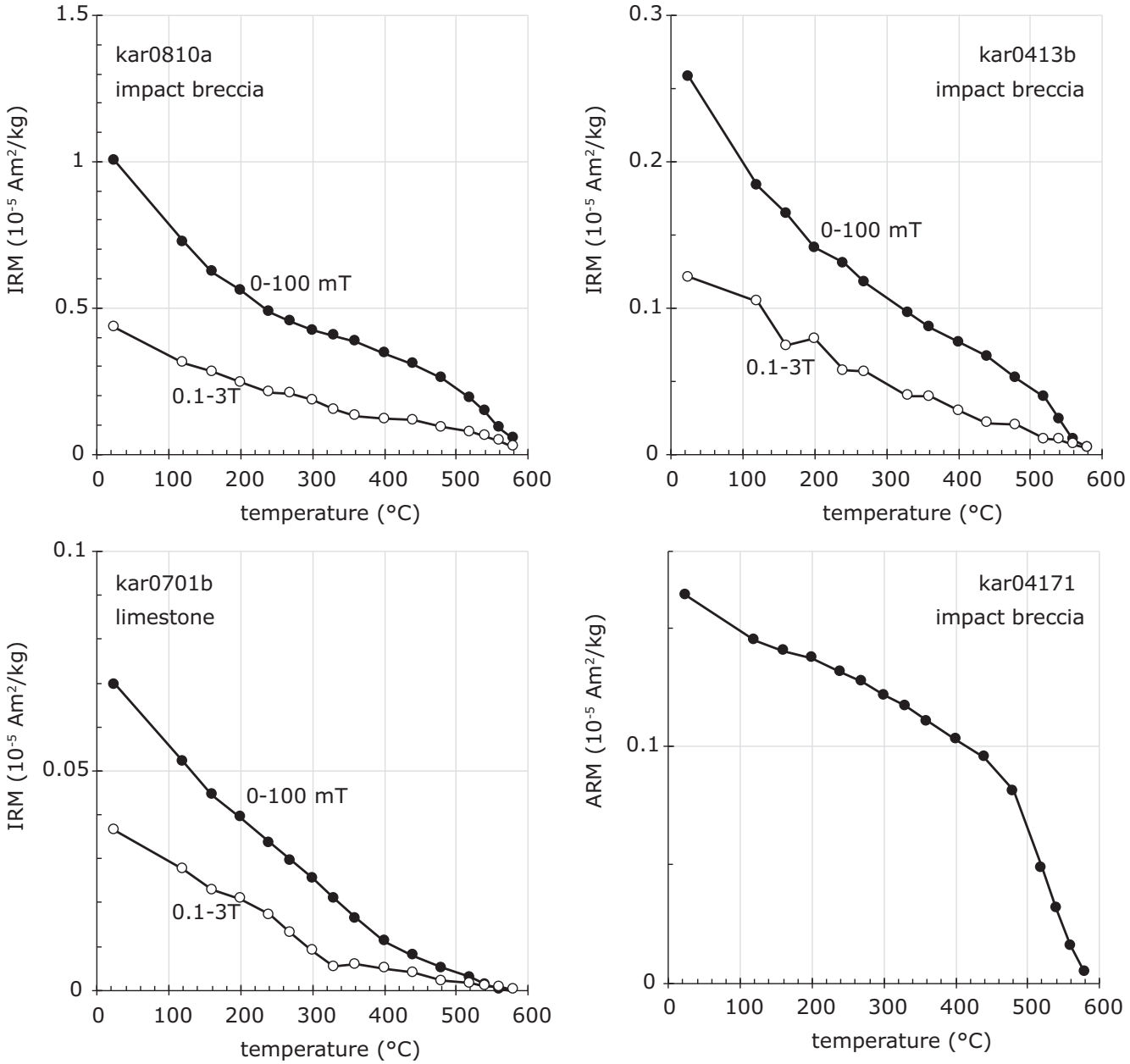

Fig. 4. Thermal demagnetization of IRM and ARM of selected samples. For IRM, two IRM were imparted along two orthogonal directions using fields of 3 T and then 0.1 T, to monitor separately the thermal demagnetization of the high- and low-coercivity grains. Demagnetization of the two IRM is shown with solid symbols (100 mT IRM), and open symbols (0.1–3 T IRM).

We focused on the specimens with the highest NRM, preferably above 3×10^{-10} Am^2. Sixteen specimens were demagnetized using thermal demagnetization, and 17 using AF demagnetization. The raw demagnetization data are provided in the supporting information (Data S2). The demagnetization data for a selection of specimens are shown in Fig. 7. After the removal of a soft overprint, stable components of magnetization were obtained for 15 samples (Table 2). They are typically unblocked up to 60–90 mT during AF demagnetization, and up to about 550 °C during thermal demagnetization (although only one sample was successfully demagnetized this way). For consistency, and to better eliminate possible viscous overprints, we included only steps for AF above 16 mT in the computation of the paleomagnetic directions. These high-coercivity and

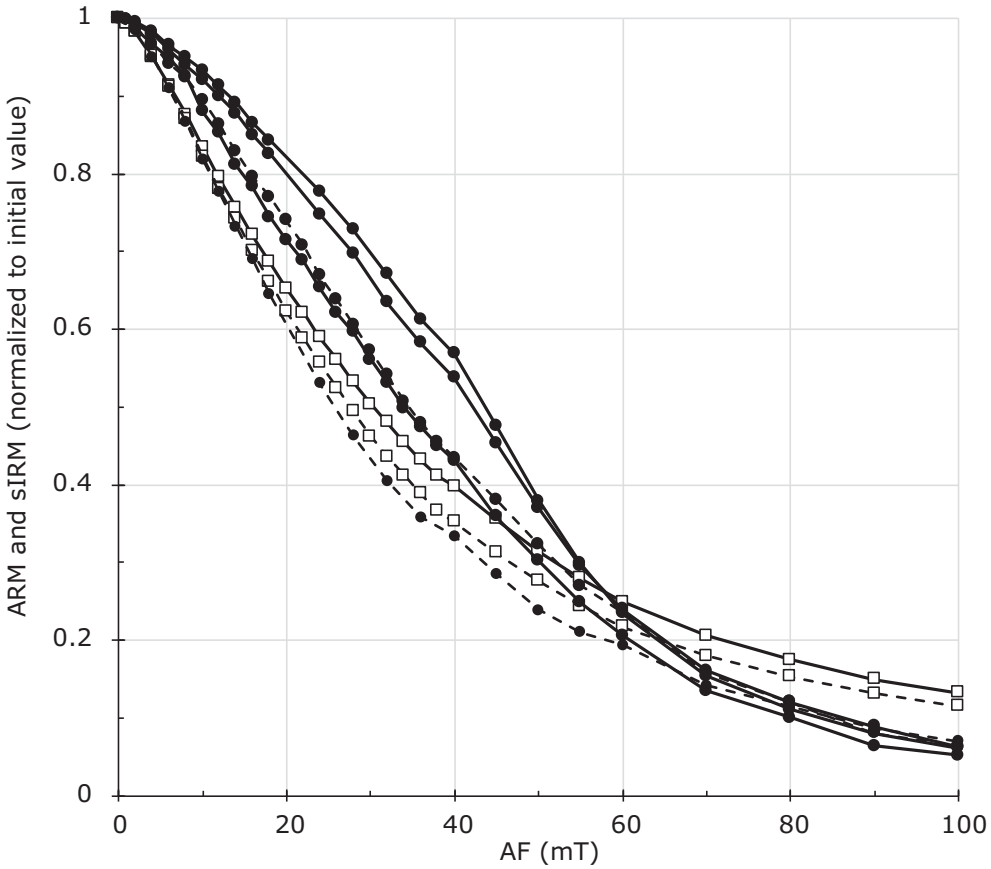

Fig. 5. AF demagnetization of sIRM (open boxes) and ARM (solid circles) of impact breccia. Solid lines are for site KAR04, broken lines are for site KAR08.

high-temperature origin-trending magnetizations are considered as the characteristic remanent magnetization (ChRM). In view of the subhorizontal bedding of the studied sites, no tilt correction was applied to the paleomagnetic directions.

DISCUSSION

Nature of the Impact Breccia

Based on the overall texture of the matrix and the euhedral shapes of calcite crystals in the matrix (Figs. 2 and 3), we suggest that this matrix was formed mostly by crystallization of a carbonate melt. Melting of calcite but not its decomposition has been observed in shock experiments (e.g., Badjukov et al., 1995), as well as in impactites from impact structures on sedimentary targets, notably at the Haughton structure (Osinski & Spray, 2001). Although most of the matrix is made of pure calcite, EDS shows that a minor fraction is enriched in Si, Al, Mg, and K, a feature that was also observed in the carbonate melt at Haughton impact structure (Osinski & Spray, 2001).

Based on the clast content and the occurrence of melt in the matrix, this breccia can be classified as a fragmental melt-bearing lithic breccia (Osinski et al., 2008). For convenience, we call it impact melt breccia in the following. We observed no significant traces of hydrothermal alteration in the studied impact melt breccia samples. Only X-ray diffraction of the residue of the breccia dissolution in HCl revealed small amounts of gypsum, bassanite, and an unidentified mica (possibly muscovite) that may be tentatively associated with hydrothermalism. However, it should be noted that bassanite may have been formed from gypsum during the drying process that followed the HCl treatment.

Intrinsic Magnetic Properties

All rocks sampled in the Karla impact structure are weakly magnetic, as indicated by low NRM, ARM, sIRM, and magnetic susceptibility (Table 1). This is

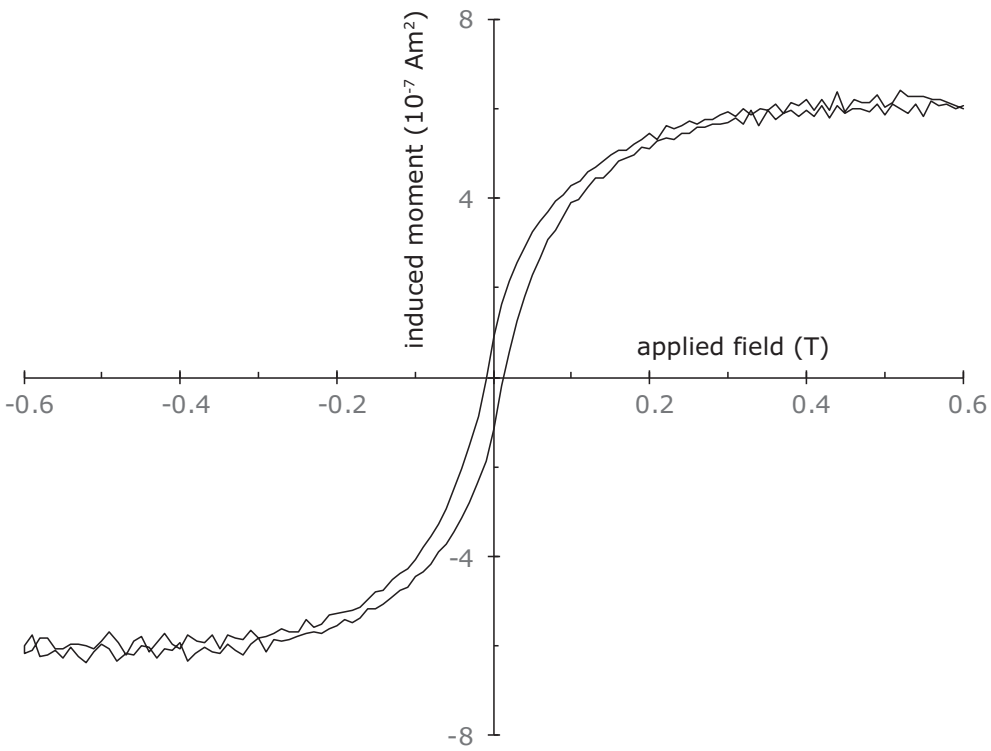

Fig. 6. Hysteresis cycle for a 947 mg aliquot of the residue of the dissolution by HCl of a bulk impact melt breccia sample from site KAR08. Applied field increment is 10 mT, and maximum field 600 mT. The hysteresis loop is corrected for the high-field susceptibility computed over the field interval 500–600 mT.

typical for platform carbonates (e.g., Lowrie & Heller, 1982). Complete demagnetization of IRM, ARM, and NRM by 580 °C strongly suggests that the main magnetic mineral in the impact breccia and the target limestones is magnetite (Fig. 4). The presence of a minor amount of pyrrhotite is suggested by a kink in the thermal demagnetization of the hard component (>100 mT) of the IRM (Fig. 5), as well as the S_{-300} ratio below 0.95 in a few limestone and impact breccia samples. The saturation magnetization and therefore the magnetite content can be estimated from the sIRM intensities coupled with the M_{RS}/M_S ratios. This value could be estimated only for the impact melt breccia with $M_{RS}/M_S = 0.21$ provided by the hysteresis measurements. The average sIRM for the melt breccia of 1.08×10^{-5} Am^2 kg^{-1} allows estimating a saturation magnetization of about 5.2×10^{-5} Am^2 kg^{-1}. Using the saturation magnetization of pure magnetite, 92 Am^2 kg^{-1} (Carmichael, 1989), and neglecting a possible small contribution of pyrrhotite, this translates into an average magnetite content of 0.6 ppm in the melt breccia, up to 0.9 ppm in the most magnetic site KAR08. The average sIRM in the limestones, 7.65×10^{-7} Am^2 kg^{-1}, is 14 times smaller lower than in the impact melt breccia, and although the M_{RS}/M_S value is not known for these rocks, it suggests a magnetite content well below 0.1 ppm.

The hysteresis parameter ratios $M_{RS}/M_S = 0.21$ and $B_{CR}/B_C = 3.1$ indicate an overall pseudo-single domain state (Dunlop, 2002). This is in agreement with the median destructive fields of ARM and sIRM (36 ± 6 mT and 29 ± 2 mT, respectively) which indicate a magnetite grain size in the range of 50 nm to 0.5 μm (Egli & Lowrie, 2002), corresponding roughly to a small pseudo-single domain grain size.

Although the magnetite content of the impact breccia is low, it is on average 14 times higher than in the target lithologies. Therefore, most of the magnetite in the impact breccia must have been formed during or after the impact. We propose two possibilities for the formation of magnetite in the impact breccia: thermal decomposition of clays due to the high temperature reached by the breccia (Hirt et al., 1993), or postimpact hydrothermalism that has been shown to be responsible for a magnetic enhancement of impact breccia in larger impact structures (Quesnel et al., 2013; Zylberman et al., 2017). The magnetite in the impact breccia is stoichiometric, as evidenced by the maximum unblocking

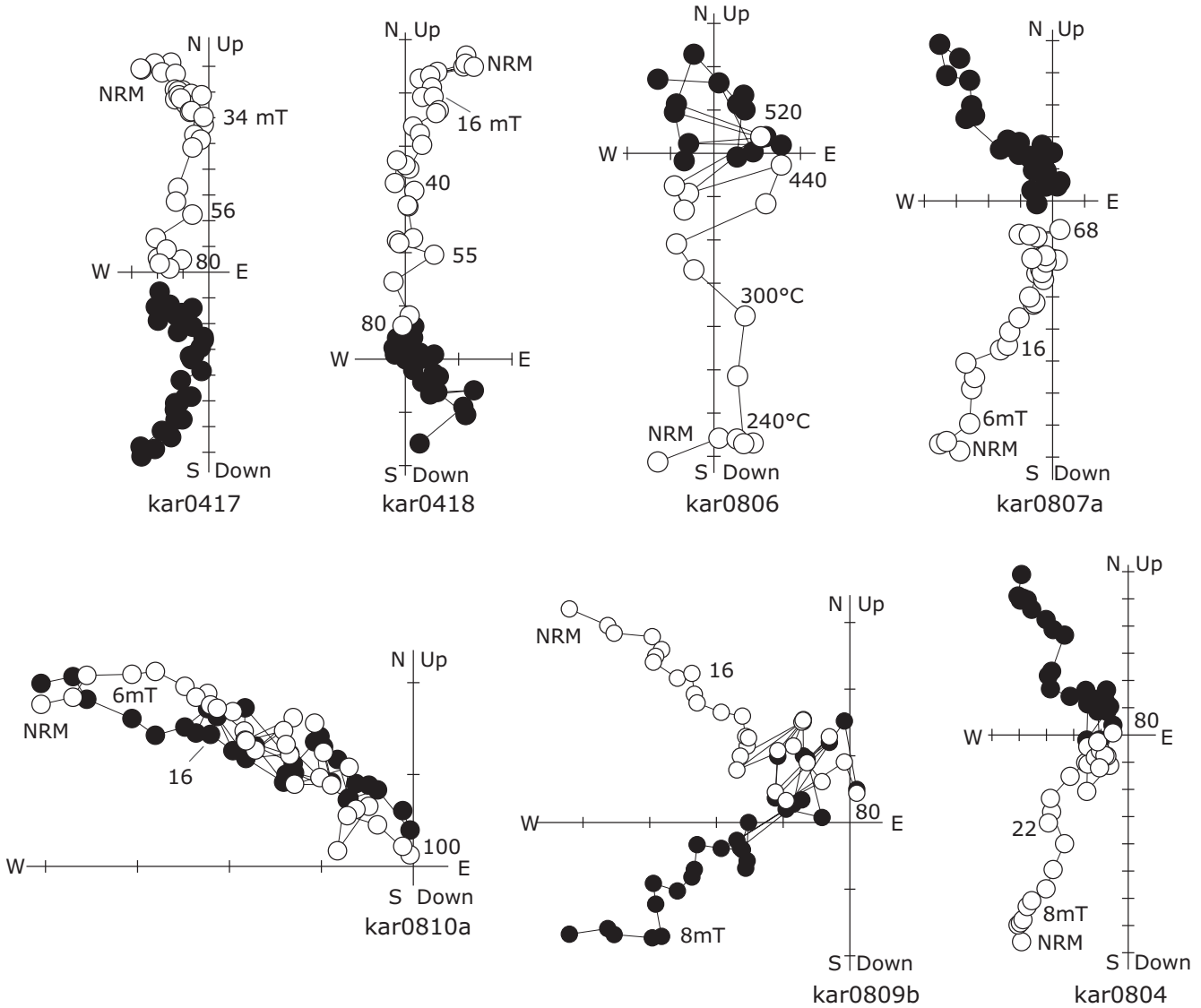

Fig. 7. Orthogonal projection plots of stepwise demagnetization data for in situ (geographic) coordinates, for selected samples. Solid and open symbols are the projection into the horizontal and vertical plane, respectively. Tick marks are 10^{-10} Am^2 on both horizontal and vertical axes.

temperature of IRM and ARM up to 580 °C, the Curie temperature of magnetite. Stoichiometric magnetite is typically formed in hydrothermal, low-temperature settings (Dunlop & Özdemir, 1997).

We observe μm-sized euhedral discrete iron oxides, possibly magnetite, associated with clay clasts (Fig. 3b), and it is noteworthy that the most magnetic impact breccias were sampled in the eastern part of the structure, where clay clasts are more abundant. The enhanced availability of iron in these may have been responsible for the enhanced formation of magnetite in the impact breccia in this part of the impact structure.

Paleomagnetism

The paleomagnetic directions obtained for 15 impact breccia samples form two roughly antipodal clusters with eight reverse polarity directions and seven normal polarity directions (Fig. 8). Directions of both polarities are found in all three sites. The reversal test of McFadden and McElhinny (1990) is negative for the overall data set. But the relatively high uncertainty on the directions, with an average maximum angular deviation (MAD; Kirschvink, 1980) of $22.5 \pm 5.5°$ makes the interpretation of the reversal test debatable.

Table 2. Paleomagnetic characteristic remanent magnetization (ChRM) directions for Karla impact breccia rocks.

Sample	NRM intensity (10^{-10} Am^2)	Steps	n	D	I (°)	MAD (°)
kar0401	2.79	20–80 mT	19	206.7	−62.2	18.5
kar0409b	0.86	20–48 mT	15	19.9	56.0	24.4
kar0413b	3.01	20–90 mT	15	296.3	62.4	32.9
kar0417	10.5	36–90 mT	14	139.3	−70.2	12.0
kar0418	5.10	16–80 mT	22	145.1	−78.0	12.0
kar0418b	3.48	16–52 mT	16	127.0	66.4	20.4
kar0802a	3.30	20–50 mT	16	222.8	−37.1	21.3
kar0804	10.4	22–70 mT	18	302.7	43.6	27.4
kar0806T	7.44	240–560 °C	11	7.5	79	25.9
kar0807a	9.45	16–56 mT	17	319.9	59.5	22.0
kar0807b	10.2	18–80 mT	21	312.5	34.0	25.3
KAR0809a	4.82	16–50 mT	18	252.1	−33.0	24.6
KAR0809b	5.55	16–80 mT	22	225.8	−17.1	27.7
KAR0810a	4.84	16–100 mT	24	293.6	−35.9	18.6
KAR0810b	5.08	16–95 mT	22	165.4	−59.2	24.8

Steps are in mT for AF demagnetization, and in °C for thermal demagnetization.
n = number of demagnetization steps used to compute the ChRM, D = declination, I = inclination, MAD = maximum angular deviation.

The average paleomagnetic direction is $D = 13.4°$, $I = 67.8°$ with $k = 5.2$, and $\alpha_{95} = 18.5°$ ($n = 15$, after transforming reverse polarity directions into normal ones). It is indistinguishable from the average dipolar geomagnetic field direction for this location ($D = 0°$, $I = 71°$). Because the apparent polar wander of the European plate has been very limited over the last 60 Myr, the paleomagnetic direction of the breccia is also undistinguishable from the expected directions computed from any European paleopoles over the period 0–60 Ma (Besse & Courtillot, 2002), which is the possible age range of the impact as constrained by stratigraphy. Therefore, the paleomagnetic results have no geochronological value, apart from pointing to an age older than the last reversal, that is, 0.8 Ma. The presence of both polarities even prevents a constraint on the impact age to a normal or reverse geomagnetic chron.

A viscous remanent magnetization origin for the ChRM is excluded by the high unblocking temperatures up to above 500 °C. Temperatures necessary to melt calcite at high pressures are in excess of 1500 °C (Osinski & Spray [2001] and references therein), well above the Curie temperature of magnetite (580 °C). Therefore, the ChRM in the melt breccia could be a thermoremanent magnetization (TRM), acquired during the cooling of the impact breccia below 580 °C. But this hypothesis is excluded by the occurrence of reverse and normal directions within the same sampling site (scale of a few meters to a few tens of meters), and sometimes within the same core (scale of a few cm). Indeed, cooling would have been identical at these spatial scales and would have resulted in a roughly contemporaneous acquisition of magnetization for all samples within a site, with identical paleomagnetic directions. Another possibility is that the ChRM is a chemical remanent magnetization (CRM) acquired during the postimpact crystallization of magnetic minerals. This process allows for small-scale variations in the timing of magnetization acquisition and therefore in the paleomagnetic direction itself. A magnetization of chemical origin is also suggested by the low ratios of NRM by ARM, and NRM by sIRM. The average ratios computed at site level are $6.05 \pm 2.24 \times 10^{-2}$ (with the ARM scaled to a 50 μT bias field) and $3.15 \pm 1.31 \times 10^{-3}$, respectively. These ratios do not show a wide spread among the studied sites with site average NRM/ARM in the 3.33×10^{-2} to 9.09×10^{-2} range, and site average NRM/sIRM in the 1.62×10^{-3} to 5.25×10^{-3} range. All these values are notably lower, by about an order of magnitude, than the typical ratios expected for a TRM acquired in a geomagnetic field of 50 μT: around 2.6 for NRM/ARM (the average TRM/ARM values for single domain/pseudo single domain magnetite bearing rocks in Yu, 2010), and 1.6×10^{-2} for NRM/sIRM (Gattacceca & Rochette, 2004), in a magnetite-bearing rock. Even if only the matrix carries the characteristic magnetization, these ratios remain representative in view of the clast abundance (about 10 vol%), and the weak remanence carrying capacity of the limestone making most of the clasts (with sIRM 14 times lower than that of the matrix). Therefore, the magnetization process that is responsible for the measured paleomagnetic signal was very inefficient with respect to thermoremanence. The

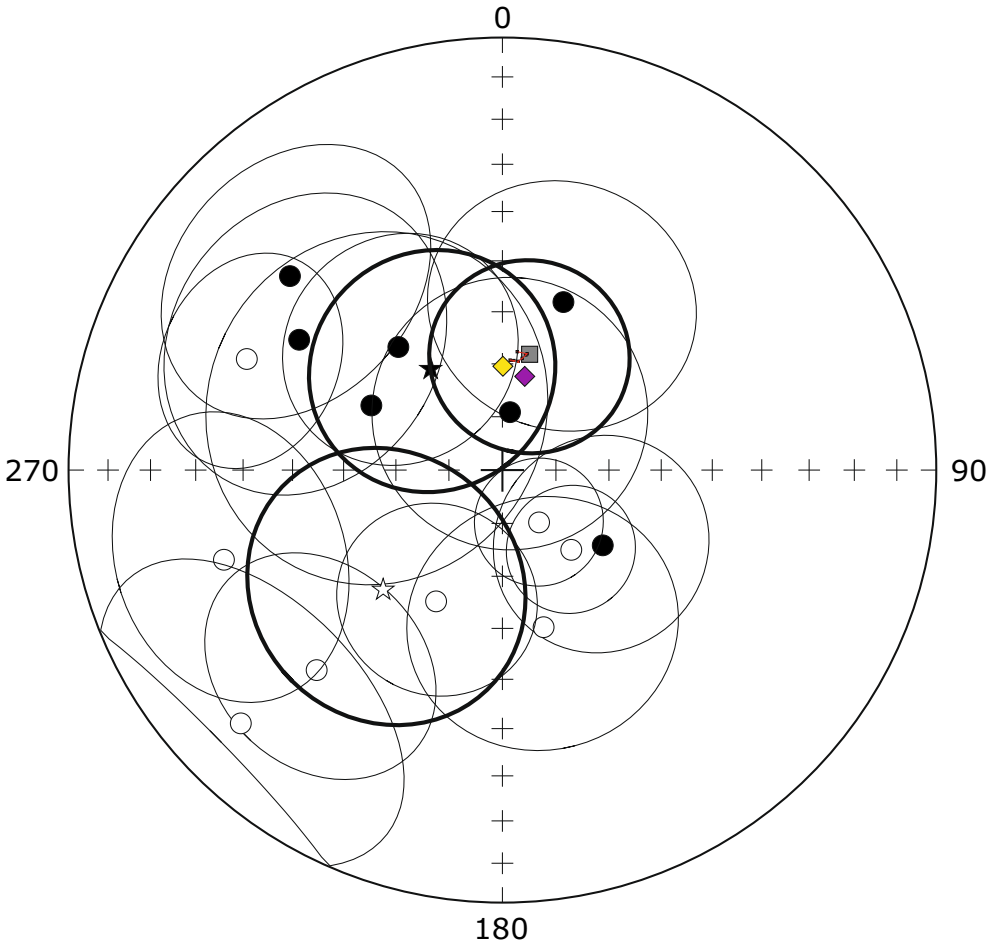

Fig. 8. Equal area stereographic projection of paleomagnetic directions. Circles are the characteristic remanent magnetization from 15 impact breccia specimens, with associated maximum angular deviation. Open symbols are upper hemisphere projections, solid symbols are lower hemisphere projections. Stars are the average directions for separate normal and reverse polarity directions with associated 95% confidence interval. The gray square is the overall paleomagnetic mean direction. The purple diamond is the present-day magnetic field at Karla structure. The yellow diamond is the dipole averaged present-day magnetic field. The red path is the expected paleomagnetic direction at Karla structure computed from the paleopoles from Besse and Courtillot (2002) for the period 0–50 Ma with steps of 10 Myr.

efficiency of CRM is not well calibrated, but it is generally assumed that it is a less efficient magnetization process than TRM (e.g., Draeger et al., 2006).

Acquisition of CRM is therefore our favored scenario for the magnetization of the impact breccia. The most plausible scenario is that the CRM was acquired during postimpact hydrothermalism, as already evidenced in larger impact structures (e.g., Zylberman et al., 2017). Indeed, no significant geological (tectonic in particular) event has taken place after the impact that could have caused the acquisition of a CRM and the associated remagnetization of the impact breccia. Because the low efficiency of magnetization excludes a thermoremanent origin, the formation of magnetite must have occurred at temperatures below the lower end of the main blocking temperature range for magnetite (~500 °C).

The nature of the remanent magnetization (CRM and not TRM) suggests a relatively low temperature of formation for the magnetite. Although our petrographic observations do not suggest the occurrence of widespread hydrothermalism in the Karla impact breccia, subtle aqueous alteration may have occurred leading to crystallization of the magnetite crystals. The occurrence of aqueous alteration in a rock emplaced at high temperature and having a bulk porosity of 31% is indeed expected. Hydrothermal alteration is therefore likely responsible for the magnetic enhancement of the breccia with respect to the target lithologies, and associated acquisition of CRM.

For the impact breccia to record paleomagnetic directions of both reverse and normal polarity, the period of magnetization acquisition must span at least over one reversal of the geomagnetic field. An alternative would be a magnetic self-reversal effect in some samples, when the rock acquired a magnetization that is antipodal to the ambient magnetic field. Such an effect has been advocated for dual magnetization polarities observed in the impact melt rocks of the Rochechouart impact structure (Eitel et al., 2014). However, this was caused by a specific magnetic mineralogy, that is, the presence of multiphase titano-hematite. The simple magnetic mineralogy in the Karla impact breccia (magnetite) does not allow the occurrence of self-reversal. The acquisition of magnetization over periods of roughly antipodal fields would also contribute to the extremely low magnetization intensities in the melt breccia, as growth of magnetite crystals during a period of a given polarity would contribute to cancel the magnetization acquired during a period of opposite polarity (e.g., Aubourg et al., 2012; Cairanne et al., 2003). Despite a limited data set, it is noteworthy that the average NRM/ARM and NRM/sIRM ratios are lower by a factor of two in the 10 reverse polarity samples than in the nine normal polarity samples. This is explained by the likely contribution to the total NRM of a minor viscous remanent magnetization (with the normal polarity of the present-day field), enhancing the NRM of normal-polarity samples, and reducing that of reverse-polarity samples. Although the paleomagnetic results cannot be used for dating the impact, the record of the two polarities of the geomagnetic field indicate that postimpact aqueous alteration affected the impact structure for a significant period of time. The duration of a geomagnetic reversal itself is of a few kyr (e.g., Simon et al., 2019), but a more relevant parameter is the average frequency of geomagnetic field reversal, which is 5 per million years over the period 5–10 Ma (from Gradstein et al., 2020). This sets the typical duration of the hydrothermal system at Karla structure to about 100 kyr.

It is noteworthy that a very similar behavior was observed in the impact breccia from the Chicxulub impact structure, with the presence of the two polarities of the geomagnetic field over small spatial scale (down to cm). These results were interpreted in the same manner, with the additional constraint of a very precise impact age that allowed setting a quantitative lower limit of 150 kyr for the duration of the hydrothermal system (Kring et al., 2020).

CONCLUSION

A layer with a maximum observed thickness of 15 m of impact breccia is found up to at least 4 km of the center of the Karla impact structure. We show that its matrix is recrystallized from a carbonate melt, implying temperature in excess of ~1500 °C. We classify this breccia as a fragmental melt-bearing breccia. It contains about 0.6 ppm of magnetite, 10 times more than any of the target sedimentary lithologies. The weak remanent magnetization and the presence of both normal and reverse polarities down to the centimeter scale indicate that the breccia does not carry a TRM, but rather a CRM. The presence of stoichiometric magnetite and the absence of TRM suggest that the magnetite was formed during postimpact hydrothermal activity occurring at relatively low temperature (well below 500 °C). This process was favored by the residual heat from the impact, the presence of a postimpact lake in the crater, and the elevated porosity of the breccia (~30%). During this process, the breccia acquired a CRM. Although the paleomagnetic direction has no dating value because of the stable position of the Eurasian plate over the last 60 Myr, the presence of both polarities indicates that mild hydrothermalism took place over a period of time long enough to span at least one reversal of the geomagnetic field, that is, over a time scale of the order of 100 kyr. This confirms that hydrothermal systems associated with impact craters are long-lived, even in relatively small crater such as Karla, and are protracted of the geologic and environmental effects of impacts on Earth.

Acknowledgments—This manuscript has benefited from constructive and detailed reviews by Phil McCausland and Thomas Kohout. This work was supported by RFBR (grant number 18-55-15014) and by CNRS Programme de Recherche Conjoint French program (grant number PRC 1975). This work was conducted under the state assignment of GEOKHI RAS. This work was supported by the Programme National de Planétologie (PNP) of CNRS-INSU co-funded by CNESfine.

Data Availability Statement—All raw data files are provided as online supplementary material files.

Editorial Handling—Dr. Gordon Osinski

REFERENCES

Abramov, O., and Kring, D. A. 2007. Numerical Modeling of Impact-Induced Hydrothermal Activity at the Chicxulub Crater. *Meteoritics & Planetary Science* 42: 93–112.

Arp, G., Kolepka, C., Simon, K., Karius, V., Nolte, N., and Hansen, B. T. 2013. New Evidence for Persistent Impact-Generated Hydrothermal Activity in the Miocene Ries Impact Structure, Germany. *Meteoritics & Planetary Science* 48: 2491–516.

Aubourg, C., Pozzi, J.-P., and Kars, M. 2012. Burial, Claystones Remagnetization and Some Consequences for Magnetostratigraphy. *Geological Society, London, Special Publications* 371: 181–8.

Badjukov D. D., Dikov Y. P., Petrova T. L., and Pershin S. V. 1995. Shock Behaviour of Calcite, Anhydrite, and Gypsum. 24th Lunar and Planetary Science Conference, pp. 63–4.

Besse, J., and Courtillot, V. 2002. Apparent and True Polar Wander and the Geometry of the Geomagnetic Field in the Last 200 Million Years. *Journal of Geophysical Research* 107: EPM 6-1–EPM 6-31. https://doi.org/10.1029/2000JB000050.

Cairanne, G., Brunet, F., Pozzi, J.-P., Besson, P., and Aubourg, C. 2003. Magnetic Monitoring of Hydrothermal Magnetite Nucleation-and-Growth: Record of Magnetic Reversals. *American Mineralogist* 88: 1385–9.

Carmichael R. S. 1989. *Practical Handbook of Physical Properties of Rocks and Minerals*. Boca Raton, Florida: CRC Press.

Cogné, J. P. 2003. PaleoMac: A Macintosh™ Application for Treating Paleomagnetic Data and Making Plate Reconstructions. *Geochemistry Geophysics Geosystems* 4(1). https://doi.org/10.1029/2001GC000227.

Draeger, U., Prevot, M., Poidras, T., and Riisager, J. 2006. Single-Domain Chemical, Thermochemical, and Thermal Remanences in a Basaltic Rock. *Geophysical Journal International* 166: 12–32.

Dressler, B. O., and Reimold, W. U. 2001. Terrestrial Impact Melt Rocks and Glasses. *Earth-Science Reviews* 56: 205–84.

Dunlop D., and Özdemir O. 1997. *Rock Magnetism: Fundamentals and Frontiers*. Cambridge: Cambridge University Press. https://doi.org/10.1017/CBO9780511612794.

Dunlop, D. J. 2002. Theory and Application of the Day Plot (Mrs/Ms Versus Hcr/Hc): 1. Theoretical Curves and Tests Using Titanomagnetite Data. *Journal of Geophysical Research* 107: 2056. https://doi.org/10.1029/2001JB000486.

Egli, R., and Lowrie, W. 2002. Anhysteretic Remanent Magnetization of Fine Magnetic Particles. *Journal of Geophysical Research* 107: 2209–EPM 2-21. https://doi.org/10.1029/2001JB000671.

Eitel, M., Gilder, S. A., Kunzmann, T., Kunzmann, T., and Pohl, J. 2014. Rochechouart Impact Melt Breccias Record No Geomagnetic Field Reversal. *Earth and Planetary Science Letters* 387: 97–106.

Escobar-Sanchez, J., and Urrutia-Fucugauchi, J. 2010. Chicxulub Crater Post-Impact Hydrothermal Activity Evidence from the Paleocene Carbonates in the Santa Elena Borehole. *Geofisica International* 49: 97–106.

Fisher, R. 1953. Dispersion on a Sphere. *Proceedings of the Royal Society of London* A217: 295–305.

Gattacceca, J., and Rochette, P. 2004. Toward a Robust Normalized Magnetic Paleointensity Method Applied to Meteorites. *Earth and Planetary Science Letters* 227: 377–93.

Gradstein, F. M., Ogg, J. G., Schmitz, M. D., and Ogg, G. M. 2020. *Geologic Time Scale 2020*. Amsterdam: Elsevier.

Hirt, A. M., Banin, A., and Gehring, A. U. 1993. Thermal Generation of Ferromagnetic Minerals from Iron-Enriched Smectites. *Geophysical Journal International* 115: 1161–8.

Kirschvink, J. L. 1980. The Least-Squares Line and Plane and the Analysis of Palaeomagnetic Data. *Geophysical Journal International* 62: 699–718.

Kring, D. A., Tikoo, S. M., Schmieder, M., Riller, U., Rebolledo-Vieyra, M., Simpson, S. L., Osinski, G. R., et al. 2020. Probing the Hydrothermal System of the Chicxulub Crater. *Science Advances* 6: 1–9. https://doi.org/10.1126/sciadv.aaz3053.

Lowrie, W., and Heller, F. 1982. Magnetic Properties of Marine Limestones. *Reviews of Geophysics* 20: 171–92.

Masaitis, V. L. 1999. Impact Structures of Northeastern Eurasia: The Territories of Russia and Adjacent Countries. *Meteoritics & Planetary Science* 34: 691–711.

Masaitis, V. L., Danilin, A. N., Karpov, G. M., and Raikhlin, A. I. 1976. Karla, Obolon, Rotmistrovka Astroblemes in European Part of the USSR (in Russian). *Doklady ANSSSR* 230: 174–7.

Masaitis, V. L., Danilin, V. N., Mashchak, M. S., Raikhlin, A. I., Selivanovskaya, T. V., and Shadenkov, E. M. 1980. *The Geology of Astroblemes*. Leningrad, Russia: Nedra Press.

McFadden, P. L., and McElhinny, M. W. 1990. Classification of the Reversal Test in Palaeomagnetism. *Geophysical Journal International* 103: 725–9.

Melosh, H. J. 2002. *Impact Cratering: A Geologic Process*, 2nd ed. New York: Oxford University Press.

Osinski, G., and Spray, J. 2001. Impact-Generated Carbonate Melts: Evidence from the Haughton Structure, Canada. *Earth and Planetary Science Letters* 194: 17–29.

Osinski, G., Tornabene, L., Banerjee, N., Cockell, C., Flemming, R., Izawa, M., McCutcheon, J., et al. 2012. Impact-Generated Hydrothermal Systems on Earth and Mars. *Icarus* 224: 347–63.

Osinski, G. R., Grieve, R. A. F., Collins, G. S., Marion, C., and Sylvester, P. 2008. The Effect of Target Lithology on the Products of Impact Melting. *Meteoritics & Planetary Science* 43: 1939–54.

Osinski G. R., and Pierazzo E. 2012. *Impact Cratering: Processes and Products*. Hoboken, New Jersey: John Wiley & Sons.

Pilkington, M., and Hildebrand, A. 2000. Three-Dimensional Magnetic Imaging of the Chicxulub Crater. *Journal of Geophysical Research* 105: 23479–92.

Quesnel, Y., Bezaeva, N., Kuzina, D. M., Rochette, P., Gattacceca, J., Uehara, M., Badjukov, D., Nasyrtdinov, B., Chareev, D., and Champollion, C. 2022. The Karla Impact Structure (Russia) as Seen by Potential Field Investigations. *Meteoritics & Planetary Science* 57: 989–1003. https://doi.org/10.1111/maps.13806.

Quesnel, Y., Gattacceca, J., Osinski, G. R., and Rochette, P. 2013. Origin of the Central Magnetic Anomaly at the Haughton Impact Structure, Canada. *Earth and Planetary Science Letters* 367: 116–22.

Schmieder, M., and Kring, D. A. 2020. Earth's Impact Events Through Geologic Time: A List of Recommended Ages for Terrestrial Impact Structures and Deposits. *Astrobiology* 20: 91–141.

Semakin, Y. G., Grishina, S. N., Vinogradov, O. R., Rudnev, M. L., Podateleva, L. P., and Balunez, Z. B. 1999. The Explanatory Note to the State Geological Map, Scale 1:200000, the Srende Volzhskay Series. N-38-XII–N-39-VII.

Simon, Q., Suganuma, Y., Okada, M., Haneda, Y., and ASTER Team. 2019. High-Resolution ^{10}Be and Paleomagnetic Recording of the Last Polarity Reversal in the Chiba Composite Section: Age and Dynamics of the Matuyama–Brunhes Transition. *Earth and Planetary Science Letters* 519: 92–100.

Simpson, S. L., Osinski, G. R., Longstaffe, F. J., Schmieder, M., and Kring, D. A. 2020. Hydrothermal Alteration Associated with the Chicxulub Impact Crater Upper Peak-Ring Breccias. *Earth and Planetary Science Letters* 547: 116425.

Yu, Y. 2010. Paleointensity Determination Using Anhysteretic Remanence and Saturation Isothermal Remanence. *Geophysics Geochemistry Geosystems* 11: Q02Z12. 10.1029/2009GC002804.

Zylberman, W., Rochette, P., Quesnel, Y., Osinski, G. R., Marion, C., and Gattacceca, J. 2017. Hydrothermally Enhanced Magnetization at the Center of the Haughton Impact Structure? *Meteoritics & Planetary Science* 52: 2147–65.

SUPPORTING INFORMATION

Additional supporting information may be found in the online version of this article.

Table S1. Porosity data for the impact breccia of Karla impact structure.

Data S1. Raw and processed X-ray diffraction data.

Data S2. Raw paleomagnetic data.